IMPROVEMENTS IN THE STRUCTURAL AND OPTICAL PROPERTIES OF IN_2O_3 NANOSTRUCTURE BY IN-SITU THERMAL ANNEALING

Azianty Saroni[1*], Saadah Abdul Rahman[2], Boon Tong Goh[2], Mahdi Alizadeh [3]

[1]*Faculty of Applied Science*
Universiti Teknologi Mara UiTM Pahang, 26400 Bandar Jengka

[2]*Low Dimensional Materials Research Centre, Department of Physics, Faculty of Science, University of Malaya, 50603 Kuala Lumpur, Malaysia*

[3]*Department of Physics, Faculty of Science, University of Zanjan, 45371-38791 Zanjan, Iran*

[*]*Corresponding author: aziantysaroni@gmail.com*

Abstract

In_2O_3/W_2N nanocomposites have been successfully grown by a single step deposition technique. The nanostructures were characterized by field emission scanning electron microscopy (FE-SEM), X-ray diffraction (XRD), Ultraviolet-Visible spectroscopy (UV-Vis), and X-ray photoelectron spectroscopy (XPS). The structure deformation of In_2O_3 nanostructure by an in-situ thermal annealing under ambient nitrogen plasma treatment was investigated. The In_2O_3 nanostructure demonstrated a decreasing in particle size when it was exposed to in- situ thermal annealing by a hot-filament at temperature of 1700 ºC. The in-situ thermal annealing enhances the surface mobility of the N adatoms to reach the nucleation sites to form crystalline W_2N. The formation of chemical composition of In_2O_3 and W_2N nanostructures presented in the material were analyzed by XPS spectra. The crystallinities of these nanostructures were revealed by XRD patterns showing the cubic, hexagonal and cubic of In_2O_3 and W_2N structures respectively. The decreasing of the optical energy gap, E_g from 2.89 to 1.69 eV which is in the visible region could be attributed to the incorporation of nitrogen into the In_2O_3 and the formation of In_2O_3/W_2N nanocomposites.

Keyword: Indium oxide, In-situ thermal annealing, Nanocomposite, Optical, Structure deformation

Introduction

In_2O_3 semiconductor materials have been investigated for their superior properties which include high conductivity (Girtan et al., 2000), high transparency in the visible region and high reflectivity in the infrared region (Zhang et al., 2016a) thus making it a promising material for transparent conducting oxides (TCOs) (Ho et al., 2011). The high conductivity, stability and suitable valence band edge for water oxidation of In_2O_3 make it a very interesting material for photo-electrochemical (PEC) application (Zhang et al., 2013). Despite of the fact that In_2O_3 is a well-established material for PEC applications, there are still several ambiguities in the understanding of energy band configuration and fundamental optical absorption in relation to the performance of In_2O_3 based PEC. Most of the In_2O_3 nanostructures to be applied in PEC application are limited by its large band gap, E_g (~ 3.75 eV) (Zou et al., 2013). Besides, it displays a typical of low quantum efficiencies owing to the short diffusion lengths of charge carriers. These could influence the photoexcitation of electron/hole pairs, the migration of charge carriers and the redox capabilities of electrons and holes in the excited state (Scaife, 1980). Moreover, the large band gap comparable to photon energy in the ultraviolet (UV)

region limits the optical absorption of solar radiation spectrum. Generally, only a small fraction of UV (< 4%) of total solar spectrum reaches the surface of the earth (Linsebigler et al., 1995) thus only a small portion of solar radiation can be utilized by In_2O_3.

Therefore, band-engineering of In_2O_3 towards producing direct and narrow bandgap In_2O_3 are more likely the solution for the material to exhibit high absorbance in the visible region and hence be suitable for the efficient harvesting of low energy photons. However, the band edge positions may not be compatible with the electrochemical potential resulting in the formation of trap states within the crystal structure which can act as recombination centres. Thus, the majority of holes created in the bulk of the material will be lost through recombination before reaching the material (electrode)/electrolyte interface. Therefore, in order to overcome the drawbacks particularly in extending the photo-response of In_2O_3 towards the visible region, In_2O_3 is combined in various forms with other narrow band gap semiconductor material. In recent years, development of nano-composites/heterojunction materials like $ZnFe_2O_4$/ In_2O_3 (Zhang et al., 2016), TiO_2/ In_2O_3 (Wu et al., 2015) and Ni-Fe/ In_2O_3-WO_3 (Chaudhari & Singh, 2017) have been reported in attempts by researchers to shift the photo-response of In_2O_3 towards the visible region for photo-electrochemical process applications.

These In_2O_3 nanocomposites have been grown by various techniques which include hydrothermal process (Zhang et al., 2016b), chemical vapor deposition (CVD) (Shen et al., 2011a) and pulsed laser deposition (PLD) (Shen et al., 2011b). Most of these techniques involve the use of high growth temperature and tedious multi-step processes in order to obtain high-crystalline nanostructure composites. The first In_2O_3/TiO_2 nanocomposites are developed by electro-deposition method (Chandra & Srivastava, 1989). This technique requires the separate growth of TiO_2 and In_2O_3 as the In_2O_3 islands are formed by first depositing indium thin film on TiO_2 by electro-deposition followed by oxidation.

In this work, In_2O_3/W_2N nanocomposites were grown at low temperature using a single step deposition technique. The nanocomposites were grown by nitrogen plasma assisted in-situ thermal annealing at filament temperatures, T_f of 1700 ºC. The effect of thermal annealing on the structural and optical properties of the nanostructures are discussed.

Materials and Methods

A home-built plasma assisted reactive thermal evaporation system was used to deposit the In_2O_3 nanostructures on p-type Si (111) substrates as explained elsewhere (Saroni et al., 2017). The filament used was a ~ 33 coiled tungsten wire (with purity of 99.95 %) with the coil diameter of ~2 mm and coil length of ~2 cm. The filament was hung by two copper electrodes at a height of 1 cm above the substrate. An In wire (with purity of 99.999 %) with diameter of 1 mm and length of 2 mm was used and placed inside the coils. Before the substrates is placed into the chamber, the substrates were cleaned followed the RCA I and RCA II cleaning procedures (Kern, 1970). Prior to the deposition, the substrates were exposed to hydrogen plasma with rf power of 15 W for 10 mins. The hydrogen flow rate and substrate temperature were fixed at 100 sccm, and 200 °C, respectively. The purpose of using the hydrogen plasma is to remove any oxide contaminations on the c-Si substrate (Jeon & Kamisako, 2008). During the deposition, the filament temperature was fixed at approximately 1000 °C in N_2 plasma ambient. The rf power, N_2 flow rate, deposition pressure and substrate temperature were maintained at 150 W, 40 sccm, 0.4 mbar and 200 °C, respectively. The in-situ thermal annealing was performed after the deposition at T_f of 1700 °C for 30 mins. The rf power, N_2 flow rate, deposition pressure and substrate temperature were fixed.

Structural morphologies of the In_2O_3 based nanocomposites was analyzed using Hitachi SU 8000 FESEM at low electron accelerating voltage of 2 kV. Crystalline patterns of the nanocomposites were obtained by PANalytical Empyrean X-ray diffractometer with the X-ray

wavelength of 1.5406 Å and the 2θ range of 20 to 80° at a fixed grazing incidence angle of 0.5°. The step time and step size of the scan was fixed at 2 seconds and 0.026°, respectively. The optical transmittance and reflectance spectra of the nanocomposites were obtained using an UV-Vis–infrared spectrophotometer (Lambda 750, PerkinElmer).The chemical states of the nanocomposites were examined by X-ray photoelectron spectroscopy (XPS, PHI Quantera II) system. A monochromatic Al K-alpha (1486.6 eV) at 25 W (15 kV and 3 mA) was used with incident angle and sample surface under base pressure at 90° and 2×10^{-7} Pa, respectively.

Result and Discussion

The comparison between the XRD patterns of the In_2O_3 nanostructure and In_2O_3/W_2N nanocomposites shown in **Figure 1**. The formation of In_2O_3 nanostructure are confirmed by the appearance of the small diffraction peaks of In_2O_3 observed at 30.5 and 50.9° which correspond to the (100) and (440) orientations, respectively [JCPDS card No. 00-065-3170. Metallic Indium (In) peaks are also observed at 32.9, 39.2, 54.5, 56.6, and 63.2° corresponding with crystallographic planes of (101), (110), (112), (200), and (103) orientations, respectively [JCPDS card No. 01-085-1409]. The formation of In_2O_3/W_2N nanocomposites occur as the nanostructures are treated by the in-situ thermal annealing at T_f of 1700 °C. A significant sharp diffraction peaks of W_2N are produced at 37.7, 43.9, 63.7, and 76.5° which are indexed to the cubic W_2N crystallographic planes of (111), (200), (220), and (311) orientations, respectively [JCPDS card No. 00-025-1257]. For the as-grown In_2O_3 nanostructures, the presence of metallic in particles indicates that the T_f was not sufficient for the in droplets to react with N or O adatoms and the short deposition time of 5 mins further reduces the possibility of any reaction. In-situ thermal annealing is needed for the as-grown sample so that the adatoms mobility is increased and the surface diffusion mechanism is thermally activated, subsequently forming the composite nanostructures.

Figure 2 shows the FESEM images of the as-grown In_2O_3 nanostructure and In_2O_3/W_2N nanocomposites prepared by plasma assisted reactive thermal evaporation and nitrogen plasma assisted in-situ thermal annealing at filament temperatures of 1700 °C, respectively. The In_2O_3 nanostructure shows the micro-grains are in irregular shape and size as illustrated in **Figure 2a**. The average size ranges from 200-300 nm with shapes of different facets (three, four, five, six, and eight faces) corresponding to triangular, rhombohedral, pentagonal, hexagonal, and octahedral shapes respectively. The formation of the micro-facets indicates that these In_2O_3 micro-grains are mostly crystalline in structure. As the nanostructure treated by the in-situ thermal annealing at 1700 °C, the nanostructure tends to change to a rhomboidal shaped grain with significant crystal facets of the crystallites as depicted in **Figure 2b**. This is attributed to the surface heating effect which initially ejecting the W adatoms from the tungsten filament as reported in our earlier work (Saroni et al., 2017). Moreover, the filament thermal irradiation results in the formation of W_2N on the surface of the In_2O_3 nanostructures.

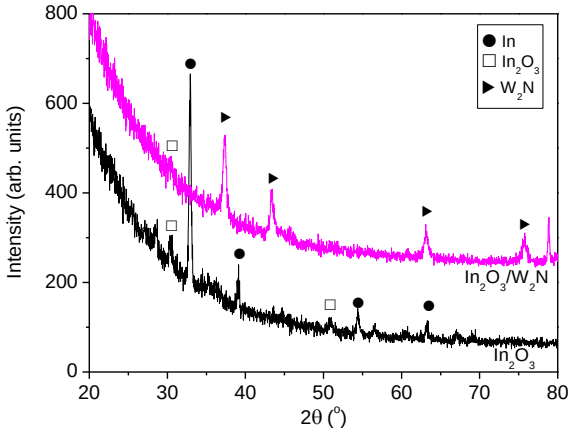

Figure 1 XRD pattern of In_2O_3 nanostructure and In_2O_3/W_2N nanocomposite

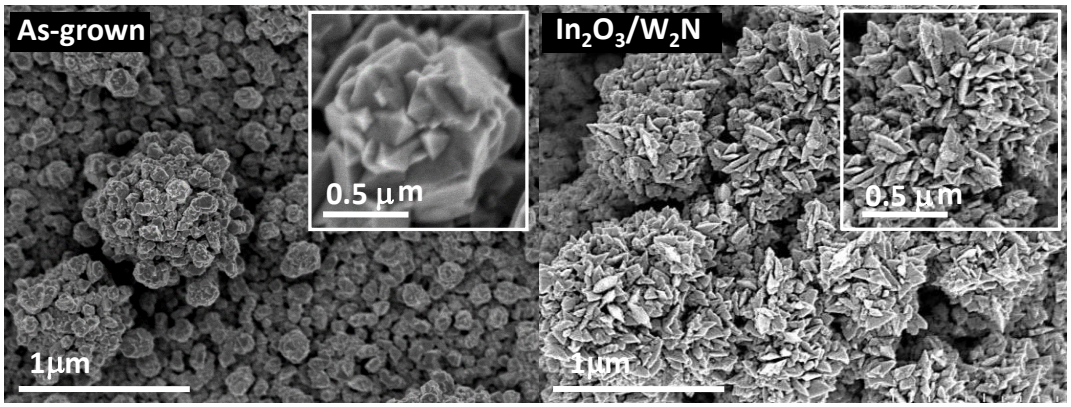

Figure 2 FESEM images of (a) In_2O_3 nanostructure, and (b) In_2O_3/W_2N nanocomposite

Figure 3 illustrates the Tauc plot of optical energy gap of In_2O_3 nanostructure and In_2O_3/W_2N nanocomposites. The result shows that the E_g value of the as-grown samples (2.89 eV) is slightly lower than that of cubic In_2O_3 nanostructure (3.75 eV) as reported in literature (Girtan et al., 2000). As the In_2O_3/W_2N nanocomposite formed, the E_g value drastically changed to 1.69 eV. Tauc plot is calculated based on transmittance and reflectance value from UV-Vis analysis as reported elsewhere (Saroni et al., 2017). The narrowing bandgap towards visible range of light is due to the presence of W_2N on the surface of the nanostructure that formed the nanocomposites. The in-situ thermal annealing leads to the increase of heating surface and thermal irradiation from the filament, that provides reactive N ions. As a result, the N ion bombardment effect leads to more N adatoms being incorporated into the nanostructures. Therefore, it tends to form W-N bonds which contributes to the narrowing of the E_g of the nanocomposites.

In order to confirm the chemical composition and purity of the as-grown In_2O_3 nanostructure and In_2O_3/W_2N nanocomposites, XPS characterization was further analysed. **Figure 4** shows the wide scan and typical deconvolution of $In3d_{5/2}$ and W4f spectra of the In_2O_3/W_2N nanocomposites. The wide scan shows the appearance of W4f peak at range 28 - 42 eV for the In_2O_3/W_2N nanocomposites while no W4f peak was observed for In_2O_3 nanostructure. This further confirms that in-situ thermal annealing leads to the formation of W_2N resulting the for mation of In_2O_3/W_2N nanocomposites. Three deconvoluted peaks of $In3d_{5/2}$ band located at 443.3, 444.5, and 445.3 eV corresponding to In-In, In-N and In-O bonds respectively

(Barick & Dhar, 2015) are observed in **Figure 4b**. The high intensity In-O peak observed from XPS in the nanocomposite annealed suggests that this peak is produced by the In_2O_3 nanostructures since In_2O_3 peak in XRD is absent for the annealed sample. This may be due to the lower crystallinity of the In_2O_3 nanostructure as confirmed by the decrease in crystallite size with introduction of in-situ thermal annealing (Saroni et al., 2017). The formation of In_2O_3/W_2N nanocomposites are further confirmed by the presence of the W4f band shown in **Figure 4c**. The W 4f band is well resolved into three component peaks in this figure. These component peaks appear as doublet peaks at 32.4 and 34.4 eV corresponding to the $W4f_{7/2}$ an d $W4f_{5/2}$ respectively of the W_2N phase (denoted as W–N bond) (Jiang et al., 2006). The W4f doublet peaks at 33.2 and 34.9 eV, and 36.2 and 38.2 eV are associated to WO_2 and WO_3 phases respectively (Jiang et al., 2006).

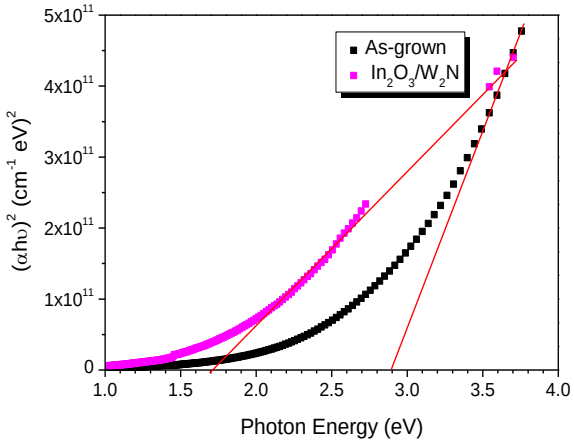

Figure 3 Tauc plot of the In_2O_3 nanostructure and In_2O_3/W_2N nanocomposite

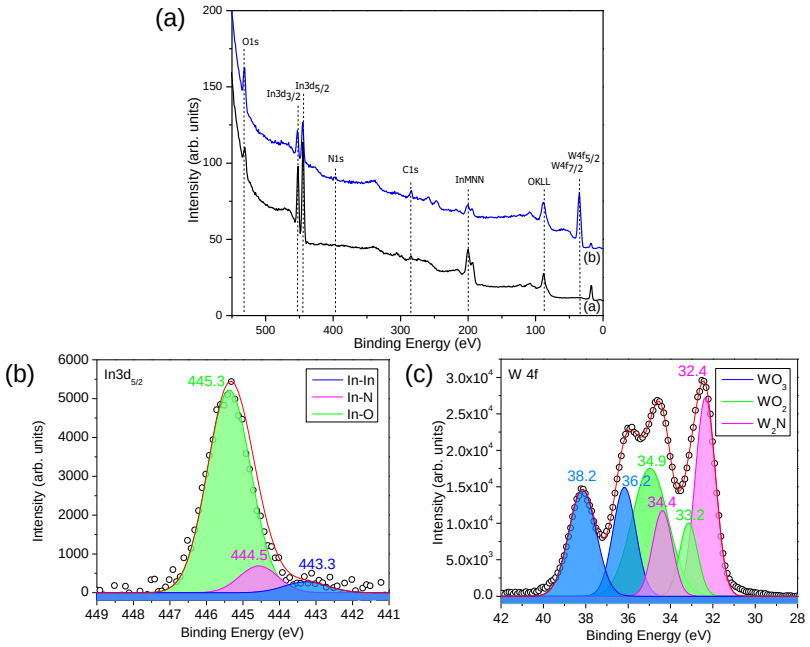

Figure 4 (a) Wide scan XPS spectra of In_2O_3 nanostructure and In_2O_3/W_2N nanocomposite, (b) Typical XPS deconvolution of $In3d_{5/2}$, and (c) Typical XPS deconvolution of W4f

Conclusion

Simple growth technique of In_2O_3 nanostructure and In_2O_3/W_2N nanocomposites have been successfully demonstrated using the plasma assisted reactive thermal evaporation and nitrogen plasma assisted in-situ thermal annealing technique, respectively. Formation of In_2O_3/W_2N nanocomposites was shown to result in a substantial decrease in the optical energy gap towards visible range from 2.89 eV to 1.69 eV of In_2O_3 nanostructure and In_2O_3/W_2N nanocomposites, respectively. The in-situ thermal annealing enhances the surface mobility of the N adatoms to reach the nucleation sites to form crystalline W_2N. This work presents a promising photoelectrochemical behaviour of In_2O_3/W_2N nanocomposites that could be applicable for photoelectrochemical applications and bring new insights into the simple growth technique of nanocomposites with superior visible light induced photoelectrochemical activity.

Acknowledgement

This work was supported by the University of Malaya High Impact Research Chancellery Grant of UM.C/625/1/HIR/237 and the University of Malaya Postgraduate Research Fund (PPP) of PG073-2015A. One of the authors, Azianty Saroni is also grateful to the Ministry of Higher Education (MOHE) and MARA University of Technology (UiTM) for the scholarship support.

Conflict of interests

We declare there is no conflict of interest.

References

Barick, B. K., & Dhar, S. (2015). Surface and bulk electronic properties of low temperature synthesized InN microcrystals. *Journal of Crystal Growth, 416*, 154-158.

Chandra Babu, K. S., & Srivastava, O. N. (1989). Structural and photoelectrochemical studies of In_2O_3 modified TiO_2 in regard to hydrogen production through photoelectrolysis. *International Journal of Hydrogen Energy, 14*(8), 529-535.

Chaudhari, A. K., & Singh, V. B. (2017). Structure and Properties of Dual Oxide Particles D oped Ni-Fe/In_2O_3-WO_3 Functional Nanocomposite Coatings. *Journal of the Electrochemic al Society, 164*(7), D371-D379.

Girtan, M., Rusu, G. I., Rusu, G. G., & Gurlui. S. (2000). Influence of oxidation conditions o n the properties of indium oxide thin films. *Applied Surface Science, 162–163*, 492-498.

Ho, C. H., Chan, C. H., Tien, L. C., Huang, Y. S. (2011). Direct Optical Observation of Band-Edge Excitons, Band Gap, and Fermi Level in Degenerate Semiconducting Oxide Nanowires In_2O_3. *The Journal of Physical Chemistry C, 115*(50), 25088-25096.

Jiang, P. C., Lai, Y. S., Chen, J. S. (2006). Dependence of crystal structure and work function of WN_x films on the nitrogen content. *Applied Physics Letters, 89*(12), 122107.

Jeon, M., & Kamisako, K. (2008). Synthesis of silicon nanowires after hydrogen radical treatment. *Materials Letters, 62*(23), 3903-3905.

Kern, W. (1970). Cleaning solutions based on hydrogen peroxide for use in silicon semiconductor technology. *RCA Review, 31*, 187-206.

Linsebigler, A. L., Lu, G., & Yates, J. T. (1995). Photocatalysis on TiO_2 Surfaces: Principles, Mechanisms, and Selected Results. *Chemical Reviews, 95*(3), 735-758.

Saroni, A., Alizadeh, M., Rahman, S. A., Dee, C. F., & Goh, B. T. (2017). Composition and optical property controlled in In_2O_3/W_2N nanostructure composites by nitrogen plasma assisted in-situ thermal annealing. *Materials Science in Semiconductor Processing, 68*, 6-14.

Scaife, D. E. (1980). Oxide semiconductors in photoelectrochemical conversion of solar energ y. *Solar Energy, 25*(1), 41-54.

Shen, G., Liang, B., Wang, X., Huang, H., Chen, D., & Wang, Z. L. (2011). Ultrathin In_2O_3 Nanowires with Diameters below 4 nm: Synthesis, Reversible Wettability Switching Behavior, and Transparent Thin-Film Transistor Applications. *ACS Nano, 5*(8), 6148-6155.

Shen. G., Xu. J., Wang. X., Huang, H., & Chen, D. (2011). Growth of Directly Transferable In_2O_3 Nanowire Mats for Transparent Thin-film Transistor Applications. *Advance Materials, 23*(6), 771-775.

Wu, J. T., Kuo, C. Y., & Wu, C. H. (2015). Synthesis of novel L-cysteine-modified TiO_2-In_2O_3 composites by the sol-gel method: evaluating surface characteristics and photocatalytic activity. *Desalination and Water Treatment, 57*(12), 5444-5451.

Zhang, B., Zhang, N. N., Chen. J. F., Hou, Y., Yang, S., Guo, J. W.,…….. Yang, H. G. (2013). Turning Indium Oxide into a Superior Electrocatalyst: Deterministic Heteroatoms. *Scientific Reports, 3*, 3109.

Zhang, F., Li, X., Zhao, Q., & Chen, A. (2016). Facile and Controllable Modification of 3D In_2O_3 Microflowers with In_2S_3 Nanoflakes for Efficient Photocatalytic Degradation of Gaseousortho-Dichlorobenzene. *The Journal of Physical Chemistry C, 120*(34), 19113-19123.

Zhang, F., Li, X., Zhao, Q., Zhang, & D. (2016). Rational Design of $ZnFe_2O_4/In_2O_3$ Nanoheterostructures: Efficient Photocatalyst for Gaseous 1,2-Dichlorobenzene Degradation and Mechanistic Insight. *ACS Sustainable Chemistry & Engineering, 4*(9), 4554-4562.

Zhang, S., Song, P., Yan, H., Yang, Z., & Wang, Q. (2016). A simple large-scale synthesis of m esoporous In_2O_3 for gas sensing applications. *Applied Surface Science, 378*, 443-450.

Ho, X., Liu, X., Wang, C., Jiang, Y., Wang, Y., Xiao, X., …… Liao, L. (2013). Controllable Electrical Properties of Metal-Doped In_2O_3 Nanowires for High-Performance Enhancement-Mode Transistors. *ACS Nano, 7*(1), 804-810.